

Machine-Learning-Based Exchange–Correlation Functional with Physical Asymptotic Constraints

Ryo Nagai^{1,2,*}, Ryosuke Akashi², and Osamu Sugino^{1,2}

¹*The Institute for Solid State Physics, The University of Tokyo, Kashiwa, Chiba 277-8581, Japan and*

²*Department of Physics, The University of Tokyo, Hongo, Bunkyo-ku, Tokyo 113-0033, Japan*

(Dated: December 2, 2021)

Density functional theory is the standard theory for computing the electronic structure of materials, which is based on a functional that maps the electron density to the energy. However, a rigorous form of the functional is not known and has been heuristically constructed by interpolating asymptotic constraints known for extreme situations, such as isolated atoms and uniform electron gas. Recent studies have demonstrated that the functional can be effectively approximated using machine learning (ML) approaches. However, most ML models do not satisfy asymptotic constraints. In this study, by applying a novel ML model architecture, we demonstrate a neural network-based exchange-correlation functional satisfying physical asymptotic constraints. Calculations reveal that the trained functional is applicable to various materials with an accuracy higher than that of existing functionals, even for materials whose electronic properties are different from the properties of materials in the training dataset. Our proposed approach thus improves the accuracy and generalization performance of the ML-based functional by combining the advantages of ML and analytical modeling.

I. INTRODUCTION

Density functional theory (DFT) [1] is a method for electronic structure. It is useful for elucidating the physical properties of various materials and plays an important role in industrial applications, such as drug discovery and semiconductor development. In principle, the electronic structure can be obtained by wave function theory (WFT), which directly solves the Schrödinger equation. However, the computational cost increases exponentially with respect to the number of electrons, which prohibits computation for materials with tens of atoms or more. Alternatively, the electronic structure can be obtained by solving the Kohn–Sham (KS) equation in DFT with a cubic computational cost [2]. This makes it possible to compute the electronic structure of materials with up to millions of atoms. As a result, DFT has become for calculating the electronic structure.

However, at the cost of the reduced computational complexity, the KS equation includes a term whose rigorous form is unknown. This term is called the exchange–correlation (XC) functional, which relates the electron density to the many-body interaction of electrons. This term has been heuristically approximated in various ways. The most common form of the XC functional is a combination of several asymptotic limits formulated with physical theories, such as the uniform electron gas limit [3]. It has been argued that satisfying as many physical constraints as possible is important to increase the performance of the approximation [4]. However, the combination of physical constraints is often performed with analytically tractable models, which may be insufficient to represent the intrinsic complexity of the XC functional.

In this context, another approach has emerged, namely, the application of machine learning (ML). By training a flexible ML model with high-quality material data, one can construct XC functionals containing more complex electronic interactions than by the analytical modeling. This approach has been demonstrated to yield successful results in various systems. [5–7] Brockherde *et al.* proposed a ML mapping to obtain electronic structures with lower computational cost than by the KS equation [6]. This method was demonstrated to be effective in accelerating materials simulations; however, it can only be applied to materials composed of the same chemical elements as those used in training. Nagai *et al.* applied ML to improve the accuracy of the XC functional in the KS equation [7, 8]. Their ML models are designed to be applicable to materials containing any chemical element; however, its performance becomes unreliable for materials that differ significantly from the materials in the training dataset. In some cases, the convergence of the calculation becomes unstable.

These problems can be solved by including all archetypal materials with all chemical elements in the training dataset; however, this is impractical because of the difficulty of obtaining such a large amount of data. Because it is difficult to obtain electronic states with sufficient accuracy via experiments, training data are mainly generated by calculation. To exceed the accuracy of conventional DFT, the data should be generated using WFT because its accuracy must be higher than that of DFT with the approximated XC functional. However, the computational complexity of modern WFT is $\mathcal{O}(N^7)$ or higher, where N denotes the system size. Thus, the materials available for training are limited to small molecules. The greatest challenge in the ML-based modeling is to achieve high generalization performance with limited data.

As a solution to this problem, a method of imposing physical constraints on ML functionals has been pro-

* r-nag@issp.u-tokyo.ac.jp

posed. Hollingsworth *et al.* imposed a physical constraint on the ML-based non-interacting kinetic energy functional in a 1D model system [9]. Without the physical constraint, the constructed kinetic energy functional could take any possible electron density as its input and predict the corresponding energy even if it did not resemble the training data. Alternatively, by imposing a coordinate-scaling condition on the density, Hollingsworth *et al.* limited the target of ML to density with a specific spatial width. By transforming the output of the ML model with the scaling condition, they obtained the kinetic energy applicable to electron densities with various system widths. Their results demonstrated that ML models with the coordinate-scaling condition learned the system with higher accuracy than ML models without constraints. This method reduced the burden on ML by compressing the dimensionality of the target system. Therefore, by introducing physical constraints appropriately, the accuracy and generalization performance of ML models can be improved.

As an extension of this approach, we propose a method to construct a ML-based XC functional for real three-dimensional materials satisfying physical asymptotic constraints. Several asymptotic dependencies of the XC functional in 3D systems have been derived analytically, which various approximate functionals have been developed to satisfy. The importance of physical constraints in improving transferability has been argued [4]. We believe that even in the construction of a ML XC functional, applying appropriate physical constraints regularize the behavior of the functional when there is insufficient training.

In this paper, we propose a novel architecture to allow a ML model to satisfy the asymptotic constraints. We apply this approach to XC functional construction based on a neural network (NN), and present training and benchmarking of the NN-based XC functional that satisfies as many physical asymptotic constraints as possible.

II. METHODOLOGY

A. Imposing Asymptotic Constraints on ML Models

Suppose that we want a ML model f to satisfy an asymptotic constraint $f(\mathbf{x}) \rightarrow f_0$ at $\mathbf{x} \rightarrow \mathbf{x}_0$. One approach is to have the training data include values at that asymptotic limit. However, ML models trained in this way do not always take the exact asymptotic value, unless the training data is strictly fitted. Alternatively, we propose making ML model satisfy the constraint in an analytical way. Instead of training the output of the ML function f directly, we train the following processed form:

$$\hat{\theta}_{\{\mathbf{x}_0, f_0\}}[f](\mathbf{x}) = f(\mathbf{x}) - f(\mathbf{x}_0) + f_0. \quad (1)$$

Here, this operation is represented by $\hat{\theta}_{\{\mathbf{x}_0, f_0\}}$. The same ML model is substituted for the first and second terms on the right-hand side. This operator forces the model to satisfy the constraint $f(\mathbf{x}_0) = f_0$ strictly.

Furthermore, suppose that we have N_c constraints, where f converges to $f_0^{(1)}, f_0^{(2)}, \dots, f_0^{(N_c)}$ at $\mathbf{x}_0^{(1)}, \mathbf{x}_0^{(2)}, \dots, \mathbf{x}_0^{(N_c)}$. We propose the following formula, which, constructed as a generalization of the Lagrange interpolation, satisfies all the constraints:

$$\hat{\Theta}_{i=1, \dots, N_c}[f](\mathbf{x}) = \sum_{i=1}^{N_c} \prod_{j \neq i} \frac{l_{i,j}(\mathbf{x} - \mathbf{x}_j)}{l_{i,j}(\mathbf{x}_i - \mathbf{x}_j)} \hat{\theta}_{\{\mathbf{x}_0^{(i)}, f_0^{(i)}\}}[f](\mathbf{x}) \quad (2)$$

Here, we represent this operation by Θ . $l_{i,j}(i, j = 1, 2, \dots, N_c)$ are function satisfying $l_{i,j}(\mathbf{x}) = 0$ at $|\mathbf{x}| = 0$. Depending on the form of $l_{i,j}$, the behavior around each asymptotic limit differs. Although further tuning can be performed, we set $l_{i,j}(x) = \tanh(|\mathbf{x}|^2)$ for all $\{i, j\}$ in this work.

B. KS Equation in DFT

Here we demonstrate the effectiveness of this architecture by applying it to the problem of constructing an XC functional. Based on DFT, the electronic structure of materials can be calculated by solving the following KS equations:

$$\left\{ -\frac{\nabla^2}{2} + V_{\text{ion}}(\mathbf{r}) + V_{\text{H}}(\mathbf{r}) + V_{\text{XC}}(\mathbf{r}) \right\} \varphi_i(\mathbf{r}) = \epsilon_i \varphi_i(\mathbf{r}), \quad (3)$$

$$V_{\text{H}}(\mathbf{r}) = \int d\mathbf{r}' \frac{n(\mathbf{r}')}{|\mathbf{r} - \mathbf{r}'|}, \quad (4)$$

$$n(\mathbf{r}) = \sum_{i=1}^{N_{\text{occ}}} |\varphi_i(\mathbf{r})|^2. \quad (5)$$

Eq. 3 is an eigenvalue equation, where the i -th eigenfunction and eigenvalue are represented by φ_i and ϵ_i , respectively. N_{occ} represents the number of occupied orbitals of the material, while V_{ion} is the Coulomb potential, which depends on the atomic position of each material. The forms of V_{H} and V_{XC} depend on the density n . The solution of this equation yields n ; however, at the same time, n is necessary for the construction of the equation itself. Therefore, the equation should be solved self-consistently; that is, the equation is solved iteratively, updating the terms using n obtained in the previous step, until n converges numerically. After solving the KS equation, the total energy E can be obtained as follows:

$$E = \sum_{i=1}^{N_{\text{occ}}} \epsilon_i - \frac{1}{2} \int d\mathbf{r} \int d\mathbf{r}' \frac{n(\mathbf{r})n(\mathbf{r}')}{|\mathbf{r} - \mathbf{r}'|} - \int d\mathbf{r} n(\mathbf{r}) V_{\text{XC}}(\mathbf{r}) + E_{\text{XC}}[n]. \quad (6)$$

TABLE I. Applied physical constraints. Numbers starting with X denote the constraints applied to the exchange part, while those starting with C denote the constraints applied to the correlation part. Items in column \mathbf{x}_0 correspond to the input of meta-generalized gradient approximation models: $(\bar{s}, \bar{\tau})$ for X, and $(\bar{n}_s, \bar{\zeta}, \bar{s}, \bar{\tau})$ for C (see Eqs. 15 and 16). Column f_0 presents the asymptotic limits that $F_{X,C}$ should converge to.

	Physical constraint	\mathbf{x}_0	f_0
X1	Correct uniform coordinate density-scaling behavior	-	(applied by Eq. 14 and 15)
X2	Exact spin scaling relation		
X3	Uniform electron gas limit	(0, 0)	1
X4	F_X vanishes as $s^{-1/2}$ at $s \rightarrow \infty$	(1, $\bar{\tau}$)	1
X5	Negativity of ε_X	-	(applied by Eq. A2)
C1	Uniform electron gas limit	$(\bar{n}_s, \bar{\zeta}, 0, 0)$	1
C2	Uniform density scaling to low-density limit	$(0, \bar{\zeta}, \bar{s}, \bar{\tau})$	$F_C^{\text{NN}}(\bar{n}_s, 0, \bar{s}, \bar{\tau}) - F_C^{\text{NN}}(0, 0, \bar{s}, \bar{\tau}) + 1$
C3	Weak dependence on ζ in low-density region		
C4	Uniform density scaling to high-density limit	$(1, \bar{\zeta}, \bar{s}, \bar{\tau})$	1
C5	Nonpositivity of ε_C	-	(applied by Eq. A2)

E_{XC} and V_{XC} are called XC functionals, and follow the relation below:

$$V_{XC}(\mathbf{r}) = \frac{\delta E_{XC}[n]}{\delta n(\mathbf{r})}. \quad (7)$$

The rigorous form of the XC functional as an explicit functional of n is unknown. In practical use, the functional is approximated in various ways [3, 10–14], and the accuracy of the DFT calculation depends on the quality of this approximation.

C. Interpreting the XC Functional as a ML Model

Here, we describe the method for constructing the ML-based XC functional. First, we divide the XC functional into exchange (X) and correlation (C) parts:

$$E_{XC}[n] = E_X[n] + E_C[n]. \quad (8)$$

Instead of taking the total X and C energy as the approximation target, we approximate the XC energy density ε_{XC} :

$$E_{X,C}[n] = \int d\mathbf{r} n(\mathbf{r}) \varepsilon_{X,C}[n](\mathbf{r}). \quad (9)$$

Subscripts “X, C” indicates the equation applies to the X and C parts, respectively. By properly constructing the local form ε_{XC} , the functional can be applied to systems of any size. Furthermore, for the convenience of calculation, most conventional studies have adopted the semilocal approximation, where $\varepsilon_{X,C}[n](\mathbf{r})$ depends locally on the electron density around \mathbf{r} . In this study, we adopt the a meta-generalized gradient approximation (meta-GGA), where $\varepsilon_{X,C}[n](\mathbf{r})$ refers to the following lo-

cal density features [12]:

$$\begin{aligned} n_s(\mathbf{r}) &= n(\mathbf{r})^{\frac{1}{3}}, \\ \zeta(\mathbf{r}) &= \frac{n_{\uparrow}(\mathbf{r}) - n_{\downarrow}(\mathbf{r})}{n(\mathbf{r})}, \\ s(\mathbf{r}) &= \frac{|\nabla n(\mathbf{r})|}{n(\mathbf{r})^{\frac{4}{3}}}, \\ \tau(\mathbf{r}) &= \frac{1}{2} \sum_{i=1}^{N_{\text{occ}}} |\nabla \varphi_i(\mathbf{r})|^2, \end{aligned} \quad (10)$$

where n_{\uparrow} and n_{\downarrow} represent the density of electrons with each spin, and $n = n_{\uparrow} + n_{\downarrow}$. Furthermore, in this work, each feature value is processed as follows:

$$\begin{aligned} \bar{n}_s(\mathbf{r}) &= \tanh(n_s(\mathbf{r})), \\ \bar{\zeta}(\mathbf{r}) &= \tanh\left(\frac{1}{2} \left\{ (1 + \zeta(\mathbf{r}))^{\frac{4}{3}} + (1 - \zeta(\mathbf{r}))^{\frac{4}{3}} \right\}\right), \\ \bar{s}(\mathbf{r}) &= \tanh(s(\mathbf{r})), \\ \bar{\tau}(\mathbf{r}) &= \tanh\left(\frac{\tau(\mathbf{r}) - \tau_{\text{unif}}(\mathbf{r})}{\tau_{\text{unif}}(\mathbf{r})}\right), \end{aligned} \quad (11)$$

where τ_{unif} is the value that τ converges to the uniform electron gas limit:

$$\tau_{\text{unif}}(\mathbf{r}) = \frac{3}{10} (3\pi^2)^{\frac{2}{3}} n(\mathbf{r})^{\frac{5}{3}}. \quad (12)$$

“tanh” conversions are used for the following reasons. First, it standardizes the features by arranging their variable range to be the same. Second, it allows us to deal numerically with asymptotic constraints at infinity. The limit $x \rightarrow \infty$ is converted to the finite limit $\tanh(x) \rightarrow 1$.

Instead of training the entire XC functional, we designed a ML model as the factor from an existing analytical functional, the strongly constrained and appropriately normed (SCAN) functional [13].

$$\varepsilon_{X,C}[n] = \varepsilon_{X,C}^{\text{SCAN}}[n] F_{X,C}[n] \quad (13)$$

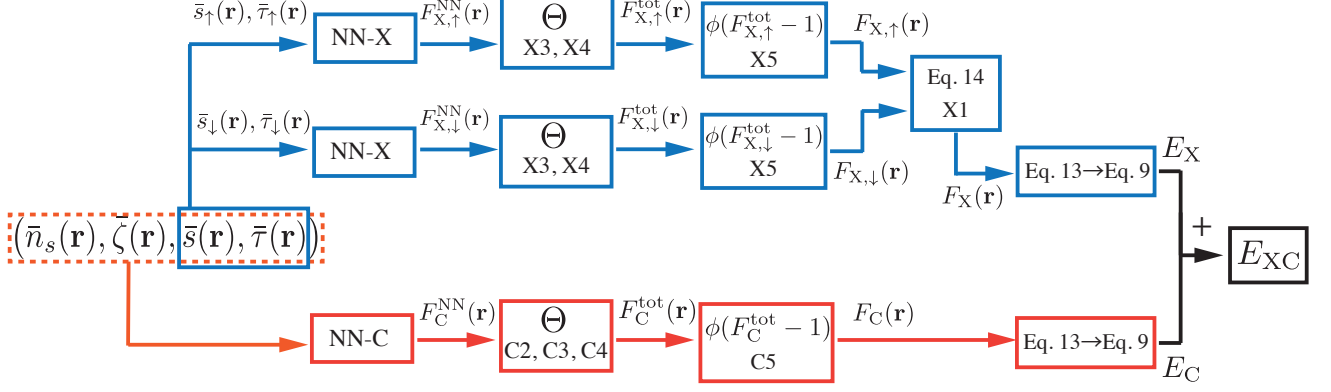


FIG. 1. Schematic diagram of the complete architecture of the physically constrained neural network XC functional. Θ represents the operation to apply the asymptotic constraints presented in Eqs. 1 and 2, while ϕ represents the activation function expressed in Eq. A1.

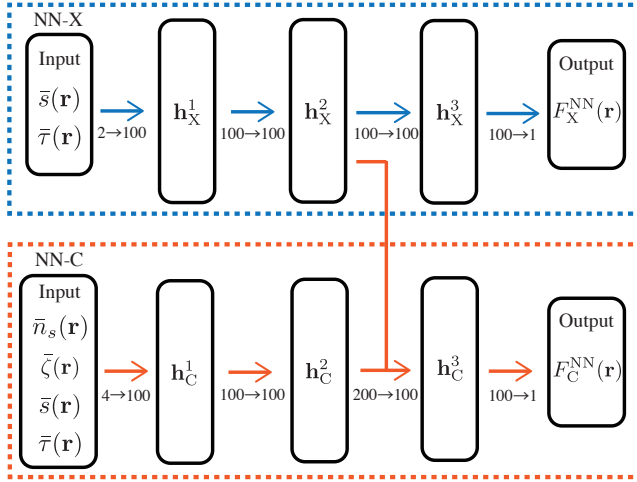


FIG. 2. Schematic diagram of the neural-network architecture. The middle layers h_X^2 and h_C^2 are concatenated to compute h_C^3 . The numbers between the layers represent the dimension of the matrices connecting the layers.

SCAN satisfies the largest number of physical constraints among existing meta-GGA approximations and is one of the most popular analytical XC functionals due to its accuracy. Using a well-constructed analytical functional can help in pre-training.

According to the correct uniform coordinate density-scaling condition [15], ε_X is independent of \bar{n}_s . Furthermore, by the exact spin scaling relation [16], the spin dependency of X energy satisfies the following relation:

$$E_X[n_\uparrow, n_\downarrow] = \frac{1}{2}(E_X[2n_\uparrow] + E_X[2n_\downarrow]). \quad (14)$$

For these constraints, we simply need to construct F_X as a function that depends only on \bar{s} and $\bar{\tau}$:

$$F_X[n](\mathbf{r}) = F_X(\bar{s}(\mathbf{r}), \bar{\tau}(\mathbf{r})). \quad (15)$$

In contrast, the C part depends on all four features:

$$F_C[n](\mathbf{r}) = F_C(\bar{n}_s(\mathbf{r}), \bar{\zeta}(\mathbf{r}), \bar{s}(\mathbf{r}), \bar{\tau}(\mathbf{r})). \quad (16)$$

In this study, we implemented $F_{X,C}$ using NNs. Here, we note that the differentiation in Eq. 7 can be implemented using automatic differentiation NN libraries. We used JAX [17] to implement the NN.

D. Imposing Physical Constraints on NN-based XC functional

Here, we demonstrate how to construct a physically constrained NN (pcNN)-based XC functional. Figures 1 and 2 present the schematic diagrams of the architecture. For both the X and C parts, we used a fully connected NN with three hidden layers, with each layer containing 100 nodes. We referred to the optimal NN size reported by Nagai et al. [8]. The middle layer of the NN of the X part was combined with that of the C part to efficiently share possible common characteristics between them.

For the constructed NNs F_X^{NN} and F_C^{NN} , we imposed the asymptotic constraints using the operation Θ . The physical constraints applied in this study are listed in Table I. Constraints X3 [3] and X4 [18] were applied for the X part, while constraints C1 [10], C2 [13], C3 [12, 19], and C4 [20] were applied for the C part. Since the XC energy density of SCAN in Eq. 13 satisfies constraints X3, X4, C1, C2, and C4, the total ε_{XC} can satisfy them by converging to $f_0 = 1$. In f_0 of the constraint C3, the output of the NN with $\bar{\zeta} = 0$ ($F_C^{\text{NN}}(\bar{n}_s, 0, \bar{s}, \bar{\tau})$) is used to suppress the ζ -dependency. By cancelling the first and second terms, f_0 converges to 1 at the low-density limit, and thus satisfies constraint C2.

E. Loss Functions

The loss function consists of the atomization energy (AE) and electron densities of H_2O , NH_3 , and CH_2 molecules, and the ionization potential (IP) of H_2O :

$$\Delta = c_1(\Delta_{\text{AE}}^{\text{H}_2\text{O}} + \Delta_{\text{AE}}^{\text{NH}_3} + \Delta_{\text{AE}}^{\text{CH}_2})/\text{AE}_0 + c_2\Delta_{\text{IP}}^{\text{H}_2\text{O}}/\text{IP}_0 + c_3(\Delta_n^{\text{H}_2\text{O}} + \Delta_n^{\text{NH}_3} + \Delta_n^{\text{CH}_2}), \quad (17)$$

where Δ_{AE} , Δ_{IP} , and Δ_n represent errors between the calculated and reference values of the AE, IP, and density, respectively. Both AE_0 and IP_0 were set to 1 hartree. In this work, the coefficients are set to $c_1 = 1$, $c_2 = 1$, and $c_3 = 10$ to make the average magnitudes of all the terms similar. The reference atomization energies, ionization energies, and electron densities were obtained by the coupled-cluster singles and doubles plus perturbative triples (CCSD(T)) method [21]. The inclusion of the electron density, a continuous quantity in 3D space, provided a large amount of information for training the weights of the NN. The error of the electron density was defined as follows:

$$\Delta_n = \frac{1}{N_e} \sqrt{\int d\mathbf{r} (n^{\text{DFT}}(\mathbf{r}) - n^{\text{CCSD(T)}}(\mathbf{r}))^2}, \quad (18)$$

where N_e represents the number of electrons of the target material. We used PySCF [22] to perform the DFT calculation to compute the energies and densities. We also used numerical integration in Eq. 18. The number of numerical grids was on average 30,000 points per molecule. Using this loss function, we trained the pcNN. See Appendix B for the detailed training procedures [23].

F. Benchmark Settings

We evaluated the performance of the trained pcNN by using it as an XC functional in the KS equation to investigate the accuracy of the electronic structure of various materials. As the test dataset, we referred to the AEs of 144 molecules, which were the same as those reported in the Training section in Ref. [24]. The DFT calculations were performed using PySCF. Additionally, because the performance for solid-state materials is also important, we conducted a test for the lattice constants of 48 solids including insulators, semiconductors, and metals, provided by [25]. The calculations for solids were performed using the Vienna Ab-initio Simulation Package (VASP) [26, 27], which is commonly used software program for calculating periodic systems. We used the pseudopotentials supplied by VASP, which are based on a projector augmented wave method and adjusted on the Perdew–Burke–Ernzerhof (PBE) functional [11, 28, 29]. For the convergence of the KS cycle, the commutator direct inversion of the iterative subspace method [30] and

TABLE II. Benchmark results for atomization energies of 144 molecules. (ME, mean error; MAE, mean absolute error; MRE, mean relative error; MARE, mean absolute relative error)

XC	ME(kcal/mol)	MAE(kcal/mol)	MRE(%)	MARE(%)
PBE	16.2	17.3	4.57	5.21
SCAN	-4.5	6.2	-1.02	2.16
NN-based	1.8	4.8	1.56	2.24
pcNN-based	-1.5	3.8	-0.30	1.74

TABLE III. Benchmark results for lattice constants of 48 solids. Parentheses in the “NN-based” row indicate that, the numerical calculations for six solids did not converge; thus, only the converged calculations were used for the statistics.

XC	ME(mÅ)	MAE(mÅ)	MRE(%)	MARE(%)
PBE	33.9	38.1	0.67	0.80
SCAN	-7.5	22.3	-0.26	0.54
NN-based	(0.8)	(22.9)	(-0.08)	(0.53)
pcNN-based	0.5	19.5	-0.06	0.46

the Pulay mixing method [31] with default parameter settings were used in PySCF and VASP respectively. The list of materials and pseudopotentials used for each element are provided in the Supplementary Information.

III. RESULTS AND DISCUSSION

Table II presents the benchmark results for molecules. We compared the performance of the XC functional constructed in this work, denoted as “pcNN-based”, with the performance of the XC functional constructed using a simple NN without satisfying any asymptotic constraints, denoted as “NN-based” [8]. Additionally, PBE and SCAN, which are widely used analytical XC functionals in practical calculations, were also compared. While the simple NN and analytical XC functionals demonstrated comparable accuracy, pcNN outperformed them even though the training dataset was almost the same as that of NN.

Table III presents the benchmark results for solids, which indicate that pcNN outperformed the other XC functionals. It is remarkable that improvements for solids were achieved using only the molecular training dataset. For both molecules and solids, the mean errors of ML-based functionals (NN, pcNN) were smaller than those of the analytical ones (PBE, SCAN). This indicates that the error of analytical functionals tend to have biased errors, whereas their ML-based counterparts yield relatively random errors even if physical constraints are imposed.

Figure 3 presents the number of iterations until the self-consistent KS cycle converged. With the NN-based functional, the self-consistent calculation was not stable and did not converge for some solids. Calculation with the pcNN-based functional, in contrast, was as stable

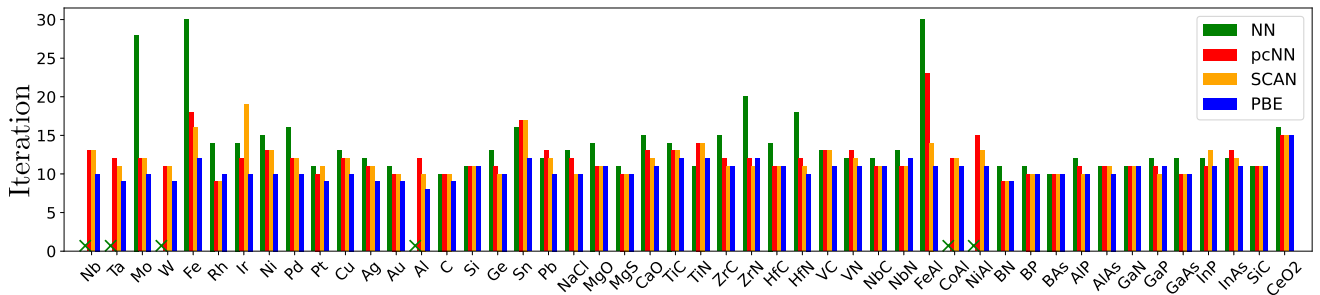


FIG. 3. Comparison of the convergence of each functional for all benchmark solids. The green x symbols indicate that the NN-based functional did not converge for the corresponding material.

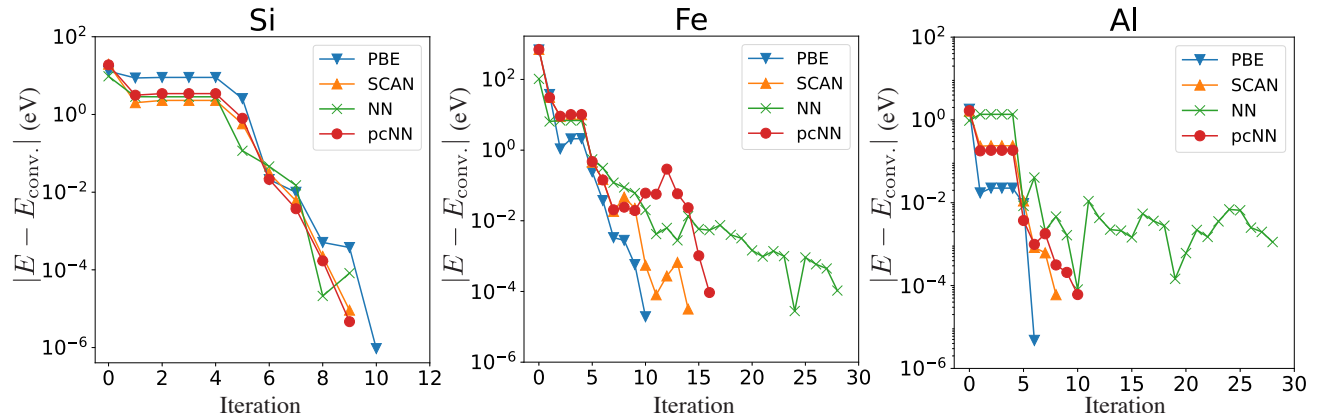


FIG. 4. Comparison of the total-energy convergence of each functional for Si, Al, and Fe. The vertical axis displays the difference between the energy of the current step and the energy of the final iteration $E_{\text{conv.}}$. The energy value at the 30th iteration was used for $E_{\text{conv.}}$ of the NN-based functional for Al as it did not converge.

as that with analytical XC functionals, even though the pseudopotentials used in the calculation were adjusted for the convergence of PBE (this was also advantageous for SCAN because its structure resembles PBE). Figure 4 illustrates the process of total-energy convergence in the self-consistent KS cycles of Si (all XC functionals converged), Fe (NN barely converged with 30 iterations), and Al (NN did not converge). When the KS calculation successfully converged, the energy difference decreased exponentially. When NN failed to converge, the total energy oscillated at certain magnitudes. The convergence of pcNN-based seems much more stable than that of NN-based, and resembles SCAN, as its structure directly included SCAN. These results suggest that if a ML functional is trained as a factor to another functional, the convergence behavior will be similar.

We argue that the improvement and stability of the pcNN-based functional were due to both the training dataset and the physical constraints. As the training dataset, we used the electronic structure of small molecules whose electrons were spatially localized. In addition, some of the asymptotic constraints imposed by the Θ operation were derived from metallic solids where electrons were delocalized (e.g., constraints X3 and C1). Thus, the pcNN-based functional was effective for both

localized and delocalized features of electrons. In the construction of the NN-based functional, the properties of the delocalized electrons were not referenced. We consider this to be the cause of the instability in the calculation of solids.

IV. CONCLUSIONS

In this study, we proposed a method to analytically impose asymptotic constraints on ML models, and applied it to construct the XC functional of DFT. Our XC functional based on the proposed NN model satisfied physical asymptotic constraints. As a result, the self-consistent solution of the KS equation converged stably and exhibited higher accuracy than existing standard XC functionals, even for solid systems that were not included in the training dataset. This improvement can be attributed to both the flexibility of the ML model and the regularization by imposing physical constraints. By incorporating these advantages, the performance of the constructed XC functional was improved.

XC functionals that have been widely used in application studies, such as PBE and SCAN, are stable and accurate for a variety of materials. One of their common

features is that they satisfy many analytic physical constraints. Similarly, pcNN is designed to satisfy as many physical constraints as possible analytically. Its high stability and accuracy are expected to be useful in practical research in the future.

The ML modeling method presented in this paper is not limited to the construction of XC functionals, but can will also be used for other ML applications where theoretical asymptotic constraints are known.

ACKNOWLEDGMENTS

This work was supported by KAKENHI Grant No. JP20J20845 from JSPS. Part of the calculation was performed at the Supercomputer System B and C at the Institute for Solid State Physics, the University of Tokyo.

Appendix A: Activation Functions

Since the variable range of the output value F is $[0, \infty)$, that of the activation function should also be semi-infinite. Additionally, it is desirable for the function to be infinitely differentiable because its derivative is substituted in the KS equation (see Eq. 7). Considering these requirements, we adopted the softplus [32] as the activation function $\phi(\mathbf{x})$ and changed its coefficients as follows to satisfy $\phi(0) = 1$ and $\phi'(0) = 1$:

$$\phi(\mathbf{x}) = \frac{1}{\log 2} \log(1 + \exp(2\mathbf{x} \log 2)). \quad (\text{A1})$$

With these adjustments, when all NN weights are set to 0, $F_{X,C}^{\text{NN}}$ converges to 1, and the total XC functional thus converges to SCAN.

Since F_X and F_C should be non-negative (see constraints X4 and C5 in Table I), these activation functions were also applied after each Θ operation (see Figure 1):

$$F = \phi(F_{X,C}^{\text{tot}} - 1). \quad (\text{A2})$$

Appendix B: Training Procedures

The loss function in Eq. 17 is computed by solving the KS equation (Eq.3) with substituting the NN-based XC functional during training. The KS equation is a self-consistent eigenvalue equation, and thus it is technically difficult to calculate its derivative. In this study, to avoid using gradients, we performed simulated-annealing-based optimization [33, 34]. We denote all the weights of the matrices and vectors in NN as \mathbf{w} . \mathbf{w} was randomly perturbed in every trial step. If NN improved the loss

value, the perturbation was accepted; otherwise, it was rejected. We set the step size of the random number generation to $\sigma = 0.003$ and the imaginary temperature to $T = 0.1\Delta_i^{t-1}$. This training was performed with 2,560 parallel threads and approximately 300 trial steps for updating per thread on a supercomputer system with AMD EPYC 7702 and 2 GB RAM per core. The overall training procedure in each parallel thread is described in Algorithm 1. After this iteration, we collected the trained weights \mathbf{w}_i^t and loss values Δ_i^t from all the parallel threads and trial steps and sorted them by Δ_i^t . For the top 100 weights, we computed the mean absolute error for the dataset consisting of the AE of 144 molecules. The molecules were small to medium-sized (the largest molecule was benzene), whose accurate WFT data are available [24]. Finally, the weights with the highest accuracy were adopted. The computational cost of this training was high because the KS equation for each material was solved in each iteration. Recently, Li *et al.* [35], Kasim *et al.* [36], and Dick *et al.* [37] implemented back-propagation of the KS equation for some systems to perform gradient-based optimization. Although we avoided using these methods owing to the lack of memory in our environment, they have the potential to improve the training efficiency.

Algorithm 1 Pipeline of training the NN in a parallel thread i .

Parameter: Step size σ , imaginary temperature T , and number of iterations N_{iter} .

- 1: Let $\mathbf{w}_i^0 = \mathbf{0}$ and $\Delta_i^0 = \infty$.
 - 2: Generate random-weight-perturbation $\delta\mathbf{w}_i^0$ from $\mathcal{N}(0, \sigma)$, where $\mathcal{N}(a, b)$ represents the normal distribution with mean a and standard deviation b .
 - 3: **for** $t = 1$ to N_{iter} . **do**
 - 4: Substitute the NN-based XC functional with parameter $\mathbf{w}_i^{t-1} + \delta\mathbf{w}_i^{t-1}$ into the KS equation and solve it for the energies and densities to calculate the loss value Δ_i^t by Eq.17.
 - 5: Compute $P = \exp(-(\Delta_i^t - \Delta_i^{t-1})/T)$.
 - 6: Generate random number $p_i^t \in (0, 1)$ from a uniform distribution.
 - 7: **if** $P > 1$ **then**
 - 8: Set $\mathbf{w}_i^t = \mathbf{w}_i^{t-1} + \delta\mathbf{w}_i^{t-1}$ and $\delta\mathbf{w}_i^t = \delta\mathbf{w}_i^{t-1}$.
 - 9: **else if** $p < P < 1$ **then**
 - 10: Set $\mathbf{w}_i^t = \mathbf{w}_i^{t-1} + \delta\mathbf{w}_i^{t-1}$ and generate the random weight perturbation $\delta\mathbf{w}_i^t$ from $\mathcal{N}(0, \sigma)$.
 - 11: **else**
 - 12: Set $\mathbf{w}_i^t = \mathbf{w}_i^{t-1}$ and $\Delta_i^t = \Delta_i^{t-1}$, and generate the random weight perturbation $\delta\mathbf{w}_i^t$ from $\mathcal{N}(0, \sigma)$.
 - 13: **end if**
 - 14: **end for**
-

[1] P. Hohenberg and W. Kohn, Inhomogeneous electron gas, Phys. Rev. **136**, B864 (1964).

[2] W. Kohn and L. J. Sham, Self-consistent equations including exchange and correlation effects, Phys. Rev. **140**,

- A1133 (1965).
- [3] J. C. Slater, A simplification of the hartree-fock method, *Phys. Rev.* **81**, 385 (1951).
 - [4] M. G. Medvedev, I. S. Bushmarinov, J. Sun, J. P. Perdew, and K. A. Lyssenko, Density functional theory is straying from the path toward the exact functional, *Science* **355**, 49 (2017).
 - [5] J. C. Snyder, M. Rupp, K. Hansen, K.-R. Müller, and K. Burke, Finding density functionals with machine learning, *Phys. Rev. Lett.* **108**, 253002 (2012).
 - [6] F. Brockherde, L. Vogt, L. Li, M. E. Tuckerman, K. Burke, and K.-R. Müller, Bypassing the Kohn-Sham equations with machine learning, *Nat. Commun.* **8**, 872 (2017).
 - [7] R. Nagai, R. Akashi, S. Sasaki, and S. Tsuneyuki, Neural-network kohn-sham exchange-correlation potential and its out-of-training transferability, *J. Chem. Phys.* **148**, 241737 (2018).
 - [8] R. Nagai, R. Akashi, and O. Sugino, Completing density functional theory by machine learning hidden messages from molecules, *Npj Comput. Mater.* **6**, 1 (2020).
 - [9] J. Hollingsworth, L. Li, T. E. Baker, and K. Burke, Can exact conditions improve machine-learned density functionals?, *J. Chem. Phys.* **148**, 241743 (2018).
 - [10] S. H. Vosko, L. Wilk, and M. Nusair, Accurate spin-dependent electron liquid correlation energies for local spin density calculations: a critical analysis, *Can. J. Phys.* **58**, 1200 (1980).
 - [11] J. P. Perdew, K. Burke, and M. Ernzerhof, Generalized gradient approximation made simple, *Phys. Rev. Lett.* **77**, 3865 (1996).
 - [12] J. Tao, J. P. Perdew, V. N. Staroverov, and G. E. Scuseria, Climbing the density functional ladder: Nonempirical meta-generalized gradient approximation designed for molecules and solids, *Phys. Rev. Lett.* **91**, 146401 (2003).
 - [13] J. Sun, A. Ruzsinszky, and J. P. Perdew, Strongly constrained and appropriately normed semilocal density functional, *Phys. Rev. Lett.* **115**, 036402 (2015).
 - [14] Y. Zhao and D. G. Truhlar, The m06 suite of density functionals for main group thermochemistry, thermochemical kinetics, noncovalent interactions, excited states, and transition elements: two new functionals and systematic testing of four m06-class functionals and 12 other functionals, *Theor. Chem. Acc.* **120**, 215 (2008).
 - [15] M. Levy and J. P. Perdew, Hellmann-Feynman, virial, and scaling requisites for the exact universal density functionals. shape of the correlation potential and diamagnetic susceptibility for atoms, *Phys. Rev. A* **32**, 2010 (1985).
 - [16] G. L. Oliver and J. P. Perdew, Spin-density gradient expansion for the kinetic energy, *Phys. Rev. A* **20**, 397 (1979).
 - [17] J. Bradbury, R. Frostig, P. Hawkins, M. J. Johnson, C. Leary, D. Maclaurin, G. Neca, A. Paszke, J. VanderPlas, S. Wanderman-Milne, and Q. Zhang, JAX: Composable transformations of Python+NumPy programs (2018).
 - [18] J. P. Perdew, A. Ruzsinszky, J. Sun, and K. Burke, Gedanken densities and exact constraints in density functional theory, *J. Chem. Phys.* **140**, 18A533 (2014).
 - [19] J. P. Perdew and Y. Wang, Accurate and simple analytic representation of the electron-gas correlation energy, *Phys. Rev. B* **45**, 13244 (1992).
 - [20] M. Levy, Density-functional exchange correlation through coordinate scaling in adiabatic connection and correlation hole, *Phys. Rev. A* **43**, 4637 (1991).
 - [21] G. D. Purvis and R. J. Bartlett, A full coupled-cluster singles and doubles model: The inclusion of disconnected triples, *J. Chem. Phys.* **76**, 1910 (1982).
 - [22] Q. Sun, T. C. Berkelbach, N. S. Blunt, G. H. Booth, S. Guo, Z. Li, J. Liu, J. D. McClain, E. R. Sayfutyarova, S. Sharma, S. Wouters, and G. K. Chan, Pyscf: The python-based simulations of chemistry framework, *Wiley Interdiscip. Rev. Comput. Mol. Sci.* **8**, e1340 (2017).
 - [23] The trained NN parameters and codes to call the XC functional are available on https://github.com/ml-electron-project/pcNN_mol (PySCF code) and https://github.com/ml-electron-project/pcNN_solid (patch program for VASP source).
 - [24] L. A. Curtiss, K. Raghavachari, P. C. Redfern, and J. A. Pople, Assessment of gaussian-2 and density functional theories for the computation of enthalpies of formation, *J. Chem. Phys.* **106**, 1063 (1997).
 - [25] P. Haas, F. Tran, and P. Blaha, Calculation of the lattice constant of solids with semilocal functionals, *Phys. Rev. B* **79**, 085104 (2009).
 - [26] G. Kresse and J. Furthmüller, Efficiency of ab-initio total energy calculations for metals and semiconductors using a plane-wave basis set, *Comput. Mat. Sci.* **6**, 15 (1996).
 - [27] G. Kresse and J. Furthmüller, Efficient iterative schemes for ab initio total-energy calculations using a plane-wave basis set, *Phys. Rev. B* **54**, 11169 (1996).
 - [28] G. Kresse and D. Joubert, From ultrasoft pseudopotentials to the projector augmented-wave method, *Phys. Rev. B* **59**, 1758 (1999).
 - [29] P. E. Blöchl, Projector augmented-wave method, *Phys. Rev. B* **50**, 17953 (1994).
 - [30] P. Pulay, Improved scf convergence acceleration, *J. Comput. Chem.* **3**, 556 (1982).
 - [31] P. Pulay, Convergence acceleration of iterative sequences. the case of scf iteration, *Chem. Phys. Lett.* **73**, 393 (1980).
 - [32] C. Dugas, Y. Bengio, F. Bélisle, C. Nadeau, and R. Garcia, Incorporating second-order functional knowledge for better option pricing, *Adv. Neural Inf. Process. Syst.* , 472 (2001).
 - [33] S. Kirkpatrick, C. D. Gelatt, and M. P. Vecchi, Optimization by simulated annealing, *Science* **220**, 671 (1983).
 - [34] V. Černý, Thermodynamical approach to the traveling salesman problem: An efficient simulation algorithm, *J. Optim. Theory Appl.* **45**, 41 (1985).
 - [35] L. Li, S. Hoyer, R. Pederson, R. Sun, E. D. Cubuk, P. Riley and K. Burke, Kohn-sham equations as regularizer: Building prior knowledge into machine-learned physics, *Phys. Rev. Lett.* **126**, 036401 (2021).
 - [36] M. F. Kasim and S. M. Vinko, Learning the exchange-correlation functional from nature with fully differentiable density functional theory, *Phys. Rev. Lett.* **127**, 126403 (2021).
 - [37] S. Dick and M. Fernandez-Serra, Using differentiable programming to obtain an energy and density-optimized exchange-correlation functional, *arXiv preprint arXiv:2106.04481* (2021).